IEEJ Journal of Industry Applications
Vol.6 No.1 pp.66–72 DOI: 10.1541/ieejjia.6.66

Paper

Frequency-Based Analysis of the Relationship between Cutting Force and CT Number for an Implant-Surgery-Teaching Robot

Koyo Yu* Non-member, Takuya Matsunaga* Student Member
Hiromasa Kawana** Non-member, Shin Usuda*** Non-member
Kouhei Ohnishi* Fellow

(Manuscript received June 11, 2016, revised Sep. 7, 2016)

An individual's feeling of bone quality during a drilling procedure is important for predicting the prognosis of a dental implant. At present, the estimation of an individual's feeling is subjective, and a new, definitive, data-based classification scheme is needed to identify bone quality objectively. A tele-robotic drilling system was developed to solve this problem. This paper presents a model for predicting vibration during bone drilling. The forces from the drill are modeled by considering the indentation process that occurs under different form computed tomography (CT) numbers. This method can be applied to a cutting-force presentation method using a haptic drilling system. An experiment was conducted to confirm the validity of the proposed method. The result shows that the experimental simulation achieved the same force response as the real cutting. The mean of the error between the real cutting force and the predicted cutting force was 3.5%. The system allows dental students to learn and practice procedures such as cutting the jaw bone. The advantages of this system are that it has a high force-output quality and a fine position-sensing ability. Therefore, dental students can simulate a realistic force response from the bone if the CT number has been acquired. This system can also be used for real implantation surgery because it allows doctors to experience the force response before operating.

Keywords: haptic, haptic dental training, CT number estimation, drilling system, motion control, vibration modeling

1. Introduction

Bone drilling is widely used in many orthopedic surgery procedures, including those for correcting bone fractures and attaching prosthetics. The desired outcome of the bone-drilling process is to produce clean and accurately positioned holes without damaging the surrounding tissue. Bone drilling is also needed in dental implantation operations. Dental implants are attracting medical attention as a treatment for missing teeth. Tooth loss has been known to leads to difficulty with mastication, decreasing the nutritional intake of vitamins and minerals. Dental implants are prosthetic devices constructed to replace missing teeth. Since the root of the implant is fixed in the jawbone just like a normal tooth, it can achieve good strength, feeling and appearance compared to traditional artificial teeth such as dentures or bridges [1].

In contrast, implant treatment requires a surgical procedure for the drilling of bone tissue. Therefore, there is a risk that such a treatment may result in subsequent complications or life-threatening accidents because of heavy bleeding or nerve damage during surgery [2]. In addition, clinical reports indicate that the 10-year survival rate of implants is only 90.5% to 96.5% [3]. Relatively large forces experienced during bone drilling pose significant challenges to the effective application of the technique. Large drilling forces and torques cause frequent drill-bit breakage [4]–[6]; since this could obstruct placement of other devices or cause adverse histological effects, follow-up procedures to remove the broken drill bit are commonly required [7][8]. Similarly, uncontrolled forces may result in drill breakthrough, imparting considerable damage to surrounding tissue [9]–[11]. Furthermore, drilling forces are the main source of heat generation during bone drilling [12] and may induce significant trauma to the tissue through osteoporosis [13][14]. Moreover, large drilling forces may promote crack formation, which can result in prosthetic or bone failure [15]. Therefore, it is critical to understand the bone-drilling process and develop functional relationships to describe the effects that drilling conditions and drill-bit geometry have upon bone-drilling forces, so as to improve drill-bit designs, select favorable drilling conditions, and assist in robotic surgery procedures [16].

For performing surgical procedures successfully, it is important to ensure that there is sufficient distance in the jawbone between the implant and anatomical landmarks, such as nerves or blood vessels. Anatomical landmarks of the jawbone include the maxillary sinus, the incisor foramen in the

* Department of System Design Engineering, Keio University
3-14-1, Hiyoshi, Kohoku-ku, Yokohama 223-8522, Japan
** Department of Dentistry and Oral Surgery, Keio University
35, Shinanomachi, Shinjyuku-ku, Tokyo 160-8582, Japan
** Tachikawa Hospital
4-2-22, Nishiki-cho, Tachikawa-shi, Tokyo 160-8582, Japan

Table 1. Conventional Method

Haptic Device	Maximum Force	Continuous Force	Position Resolution	Stiffness	DOF
Desktop (Wu)	7.9 N	1.75 N	23 μm	2.4 N/mm	3 DOF
Omni (Rhienmora)	3.3 N	0.88 N	55 μm	2.3 N/mm	3 DOF
Premlum1.5 (Laehyun)	8.5 N	1.4 N	30 μm	3.5 N/mm	6 DOF
Proposed Method	78.0 N	20.0 N	0.1 μm	11 N/mm	1 DOF

maxilla, the mandibular canal, and the incisive foramina in the mandible. Ingression of these landmarks may cause nerve damage or heavy bleeding. Therefore, the implant must have a margin of at least 2 mm from each of these landmarks. In addition, the jawbone should have sufficient bone density to hold the implant to ensure the long-term success of prosthesis [17].

Because the top of the drill is invisible during an operation, physicians must perform the surgery based on delicate feelings from the cutting device. To correctly handle this device, physicians must rely on advanced techniques and extensive experience. As the quality of operation depends on the skills of the physician, lack of experience may result in damage to a the jawbone landmark due to over-cutting the depth that was set in advance.

To protect patients from such medical accidents, it is necessary to eliminate the health disparities that arise from varying levels of physician experience. The research and development of a supporting technology for the physician can prevent the occurrence of medical accidents.

Table 1 shows the performance of the conventional method. Wu et al. applied a half-silvered mirror and a Phantom Desktop device in their realization of a dental-training system [18]. Kim et al. and Rhienmora et al. also used visual, auditory, and haptic display systems such as Phantom Premium or Phantom Omni to construct dental workbenches [19][20]. However, the continuous force performance of these conventional methods is relatively low (1.75 N for Phantom Desktop, 0.88 N for Phantom Omni, and 1.4 N for Phantom Premium). The required continuous-force performance is 8.0 N or more when cutting a cortical bone (0.6 mm/s) and 20.0 N when a cutting porcine lower jaw bone [21]. Therefore, the performance of the conventional method is too small to realize a force response when cutting bone tissue.

In this paper, a novel design for a cutting-force presentation method using a haptic drilling system is presented. This system allows dental students to learn and practice procedures such as cutting the jaw bone. The advantages of this system are that it has a high force-output quality (20.0 N in continues) and a fine position-sensing quality (0.1 μm). Therefore, dental students can simulate realistic force responses from a bone if the computed tomography (CT) number has been acquired. This system can also be used for real implant surgery because it allows doctors to experience force response prior to an operation. The final goal of this research is to achieve real-time CT number estimation estimation using five degree of freedom robot arm in last study [22] and an automatic stop system using bilateral control. In this paper, the cutting force and motor vibration are modeled as one equation using a discrete Fourier transform (DFT). The motor vibration is normalized by the cutting force to avoid interference between the CT-based parameter identification and the cutting-vibration data.

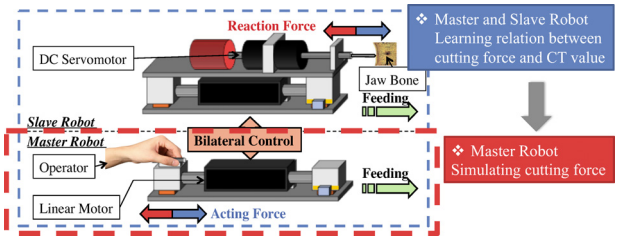

Fig. 1. Concept of robotic drilling system

2. Materials and Methods

Figure 1 shows the concept of robotic drilling system and Fig. 2 presents a flow diagram of the proposed method. This system makes use of master and slave robots. The master robot can be operated by the physician, and whereas the slave robot interacts with the environment. The forces and positions of the master and slave robots are transmitted in both directions by a bilateral control [23].

The slave robot is used to learn the relationship between the cutting force and the CT number. Then, the master robot is used to simulate the cutting force. The relation between the cutting force and the CT number is given by Eq. (1); it has the same structure as DFT:

$$F^{res} = s_t \left(A_0(C_T, \dot{x}) + \sum B_n(C_T, \dot{x}) \exp(2\pi i f_n t) \right), \quad \cdots\cdots (1)$$

where s_t is a rate of cutting width w to the real length of cutting blade w_c. It changes in the range from 0 to 1 depending on the drilling states shown in Fig. 4, and f_n is the dominant frequency when cutting the material. A_0 is the zero-frequency term that indicates the magnitude of the signal, and B_n is the n-frequency term, which has an imaginary value. A_0 and B_n are functions of the CT number C_T and the velocity $\dot{x}$. The aim of this paper is find the shape and value of the A_0 and B_n.

2.1 Drilling States and Continuous Force

In this section the shape of s_t will be explained. Figure 4 shows the head of the twist drill. The continuous force changes depending on the cutting width, and there are three states when cutting bone-like material.

(I) Contact with the Material:
The cutting width w increases in proportion to the cutting depth, x. Therefor, $w \cdot l_t / w_c$ is equal to the cutting depth x, and the continuous force F^{res} increases in proportion to x. s_t in this state is shown in Eq. (2):

$$s_t = \frac{x}{l_t}. \quad \cdots\cdots (2)$$

Here, l_t represents the length of the drill top.

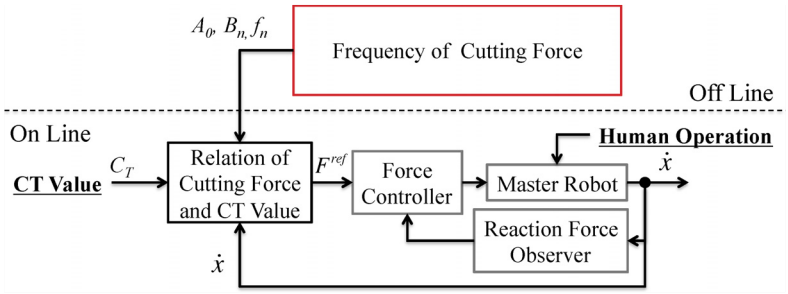

Fig. 2. Proposed method

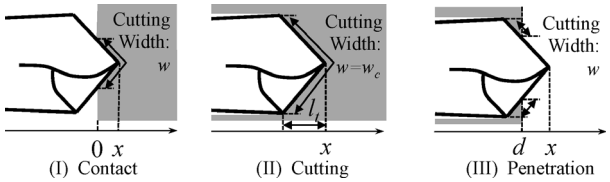

Fig. 3. Drilling states

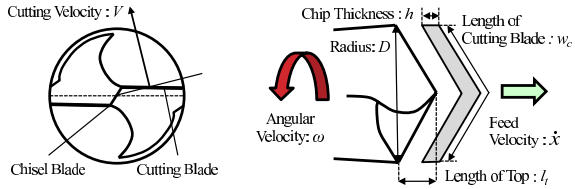

Fig. 4. Head of the twist drill

(II) Cutting the Material:
The cutting width, w, is equal to the length of cutting blade, w_c. Thus, the continuous force, F^{res}, is not changed by the cutting depth. s_t in this state is shown in Eq. (3):

$$s_t = 1. \cdots\cdots (3)$$

(III) Penetrating the Material:
The cutting width, w, changes depending on the rate of the cutting material and the air with which the cutting edge makes contact. Therefore, the continuous force decreases to 0 as x increases to $d + l_t$. s_t in this state is shown in Eq. (4):

$$s_t = 1 - \frac{x-d}{l_t}, \cdots\cdots (4)$$

where d represents the depth of the cutting material.

2.2 Material Density and CT Number The shape of the chip formed by drilling is important for determining the continuous force. For example, the shape of the chip in metal cutting is continuous. In this case, the continuous force can be calculated from the geometric structure of the cutting blade and the cutting material.

However, when cutting fragile materials such as bone or wood, the shape of chip is cracked. In this case, it is almost impossible to calculate the continuous force from the geometrical structure, because the shapes and sizes of the chips are randomly generated.

Although the continuous force cannot be calculated from the geometrical structure of the cracked chip, some experimental observations may be of help. For example, the continuous force, F, is expressed as a function of the material density, δ, to the power of n. This relation can be written as Eq. (5):

$$F = K_d \delta^n (1 + K_e \dot{x}). \cdots\cdots (5)$$

This equation constitutes the relationship between material density and continuous force. The functions A_0 and B_n in Eq. (1) have the same shape of F in Eq. (5).

CT produces volumetric data of various bodily structures based on their ability to block X-ray beams. The CT number is the relative value normalized by the values for water (0 HU) and air (−1,000 HU). For example the CT number of fat is around −100 HU, that of muscle is around 60 HU to 70 HU, and the that of bone is around 200 HU to 2,000 HU.

The CT number is proportional to the material density, δ, and the mass-attenuation coefficient, ζ, which are the unique for each material. The relationship between these quantities is as follows Eq. (6):

$$\zeta\delta = C_T - 1000 = C'_T. \cdots\cdots (6)$$

The relationship between the force, F, and CT number, C_T, can be written as Eq. (7) based on Eq. (5) and Eq. (6):

$$F = \frac{K_d}{\zeta^n} {C'_T}^n (1 + K_e \dot{x}). \cdots\cdots (7)$$

2.3 Model of Cutting Vibration Motor-vibration information is also an important consideration in drilling. Physicians must feel not only the force feed-back, but also the vibration of the motor to detect the hardness of the cutting environment.

Motor vibration data are acquired from a fast Fourier transform and can be modeled as the sum of trigonometric functions given by Eq. (8):

$$F_{vib} = \sum B_n \exp(2\pi i f_n t). \cdots\cdots (8)$$

The amplitude, $|B_n|$, and the dominant frequency, f_n, are important for obtaining the equation of the cutting force. In the experiment, the gain of RFOB g_r was set to 1,000 rad/s. The cut off frequency of RFOB can be calculated as Eq. (9):

$$\frac{g_r}{2\pi} = 159\,\text{Hz}. \cdots\cdots (9)$$

The Nyquist frequency can be calculated from the sampling time, t_s(0.1 ms), as Eq. (10):

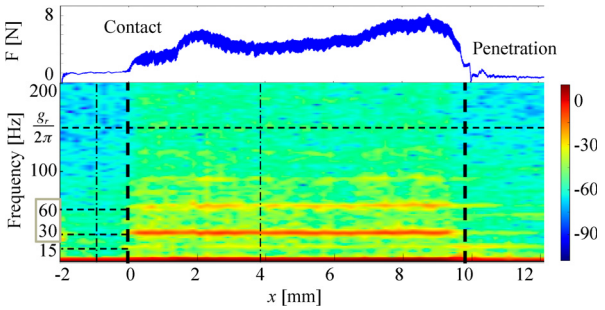

Fig. 5. Force spectrogram obtained during cutting of pine wood

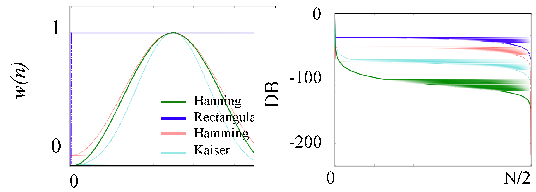

(a) Shape (b) Amplitude

Fig. 6. Window function

$$\frac{1}{2t_s} = 5000\,\text{Hz}. \cdots\cdots (10)$$

The observed cutting-vibration frequency is smaller than both the cut-off and Nyquist frequencies.

2.4 Frequency Analysis Figure 5 shows a spectrogram obtained under cutting of pine wood. A small 15 Hz vibration is generated under free motion, but the amplitude is very small. On the other hand, 30 Hz combined with 60 Hz vibration are generated during cutting motion, and these amplitudes are sufficiently large.

The free-motion vibration frequency remains 15 Hz when the angular velocity is 900 rpm. 30 Hz is the dominant frequency during all drilling states; this is because the drill head has two cutting blades. 60 Hz is the second most dominant frequency. However, the amplitude is about one fifth that of the 30 Hz mode. The amplitude of the 90 Hz mode is too small to be recognized from the noise. Therefore, we can choose 30 Hz and 60 Hz as dominant frequency.

2.5 Window Function A discrete Fourier transform (DFT) is a general definition for complex inputs and outputs. The analysis is usually done by applying a window function. Figure 6 shows several kinds of window function, including rectangular, Hanning, Hamming, and Kaiser windows. THe rectangular window is the simplest window, given by Eq. (11):

$$w(n) = 1. \cdots\cdots (11)$$

It is equivalent to replacing all but N values of a data sequence with zeros. It has a property by which the waveform suddenly appears to turn on and off, creating a high folding noise.

The Hanning window is typically used as a window function in digital signal processing to select a subset of a series of samples, as shown by Eq. (12). There is almost no folding noise using a Hanning window.

$$w(n) = 0.5 - 0.5\cos\frac{2\pi n}{N-1}. \cdots\cdots (12)$$

Figure 6(b) shows the amplitude of the window function. The ideal response is for all values to be 0. From Fig. 6(b), the Hanning window has the lowest error.

3. Results

In this section calibration and experimental simulation will be described. First, the experimental results are shown to identify the parameter in the equation of the cutting force as well as the CT number. Next, experimental results are presented to confirm the validity of the proposal.

The material properties of bones obtained by standard (e.g., tensile) testing method are highly inaccurate for the ranges of strains σ (> 1) encountered during bone drilling [25]. Similarly, the effective friction conditions between the chip and the drill bit (rake face) are not well known. For these reasons, a mechanistic approach is used here to model the bone-drilling process, whereby the amplitudes of each dominant frequency mode, f_n, are taken into account empirically through calibration tests. The dependence of the amplitude of the cutting vibration can be represented effectively via a dB scale using the feed velocity and CT number as parameters. The dB-scale relationship can be expressed as a linear equation in the logarithmic domain given by Eq. (13):

$$\log F = b_{n0} + \log(1 + K_e\dot{x}) + n\log C'_T, \cdots\cdots (13)$$

where F is A_0 and B_n, $\dot{x}$ and C'_T are the feed velocity and CT number, respectively, and the b terms are calibration coefficients. An attractive aspect of this dB-scale model is that it requires only a small number of tests to determine the calibration coefficients. The calibration parameters are valid within the ranges used in the calibration experiments. Different drill-bit geometries and drilling conditions can be accommodated using the same calibration data. The use of carbide drill bits instead of stainless steel drill bits would result in somewhat different calibration values; however, the calibration procedure would remain the same. Similarly, the calibration values would change if different objects were to be considered. Figure 7 and Fig. 8 show the amplitudes of A_0 and of $|B_{30}|$ and, $|B_{60}|$, respectively.

3.1 Calibration Results Under Experiments at Various Velocities An experiment was conducted in which the slave robot was used to cut pine wood in cutting the same CT number area. The feed velocity was ranged form 0.1 mm/s to 0.5 mm/s. Data were collected for cutting depths between 1 mm and 8 mm. In this experiment, the CT number was a constant parameter. Therefore, $b_{n0} + n\log C'_T$ could be considered as a constant parameter b'_n and Eq. (13) could be calculated as Eq. (14). When $K_e\dot{x}$ is nearly zero, Eq. (14) can be approximated as Eq. (15):

$$\log F = b'_n + \log(1 + K_e\dot{x}) \cdots\cdots (14)$$

$$\approx b'_n + \frac{K_e}{\ln 10}\dot{x}. \cdots\cdots (15)$$

Figure 9 shows the relationship between A_0 and $\dot{x}$; Fig. 10 shows the relationship between $|B_{30}|$, $|B_{60}|$ and $\dot{x}$. Table 2 shows the parameter-calibration results for the experiments under various velocities. Figure 9 indicates that there is almost no correlation between the feed velocity and the amplitude of the dominant frequency mode, because the parameters K_e are approximately equal to 0. Therefore, K_e is set to

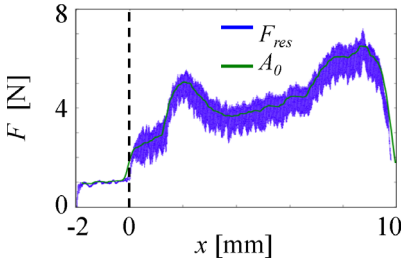

Fig. 7. Amplitudes of A_0

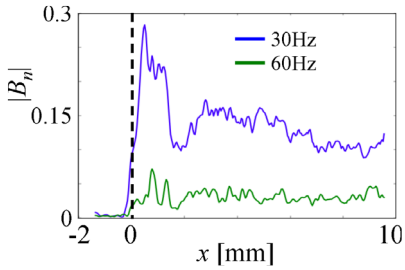

Fig. 8. Amplitudes of $|B_{30}|$ and $|B_{60}|$

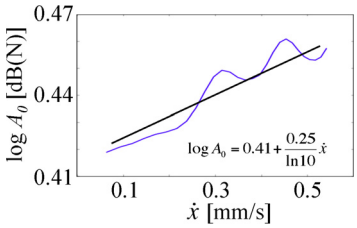

Fig. 9. Relationship between A_0 and $\dot{x}$

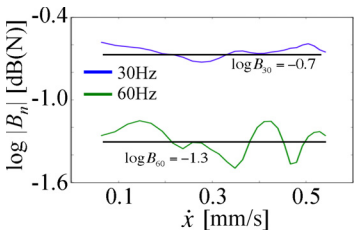

Fig. 10. Relationship between B_n and $\dot{x}$

Table 2. Results for velocity calibration

	Caption	Value	error (%)
A_0	b'_n	0.41	2.1
	K_e	0.25	8.5
B_{30}	b'_n	−0.70	7.2
	K_e	0	-
B_{60}	b'_n	−1.3	9.6
	K_e	0	-

0 in this system.

3.2 Calibration Results Under a Constant-velocity Experiment An experiment was conducted using the slave robot to cut pine wood with a constant feed velocity (0.4 mm/s). The experiment was conducted five times. The data were recoded for cutting depths between was 1 to 8 mm.

In this experiment, the velocity was a constant parameter. Hence, $b_{n0} + \log(1 + K_e\dot{x})$ could be considered as a constant parameter b''_n and Eq. (13) could be calculate as Eq. (16):

$$\log A_0 = b''_n + n \log C'_T, \cdots\cdots\cdots\cdots\cdots\cdots\cdots\cdots (16)$$

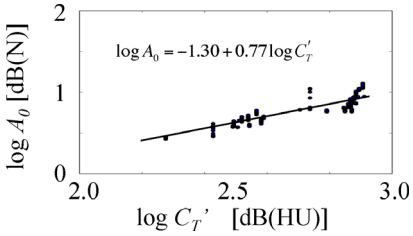

Fig. 11. Relationship between A_0 and C'_T

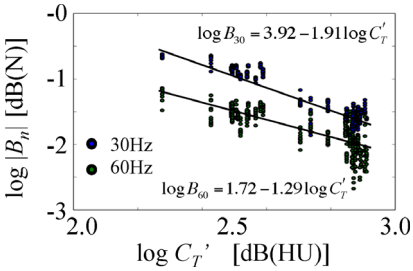

Fig. 12. Relationship between B_n and C'_T

Table 3. Results of CT calibration

	Caption	Value	error (%)
A_0	b''_n	−1.30	3.75
	b_{n0}	−1.35	-
	n	0.77	2.35
B_{30}	b_{n0}	3.92	2.68
	n	−1.91	2.05
B_{60}	b_{n0}	1.72	7.87
	n	−1.29	3.90

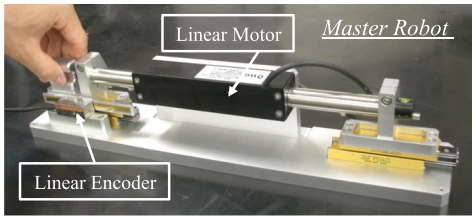

Fig. 13. Master robot

where b_{n0} can be obtained by Eq. (17):

$$b''_n = b_{n0} + \frac{K_e}{\ln 10}\dot{x}. \cdots\cdots\cdots\cdots\cdots\cdots\cdots\cdots (17)$$

With the results from last section, Eq. (13) for $|B_{30}|$ and $|B_{60}|$ can be written as Eq. (18).

$$\log B_n = b_{n0} + n \log C'_T. \cdots\cdots\cdots\cdots\cdots\cdots\cdots\cdots (18)$$

Figure 11 shows the relationship between A_0 and C'_T, Fig. 12 shows the relationship between B_n and C'_T, and Table 3 shows the parameter-calibration results for the constant-velocity experiment.

3.3 Experiment In this section, the experiments conducted in this paper are described and the validity of the proposal is confirmed.

3.4 Experimental Setup The master robot of the experimental system is illustrated in Fig. 13. This robot consists of a linear motor. RFOB was implemented on the linear motor to estimate the applied external force [24]. The coulomb friction force was found to be 1.0 N by a pre-experimental observation. The parameters for the linear motor are listed in Table 4.

Table 4. Parameters of linear motor

Parameters	Description	Values
M_{nm}	Nominal mass of Master	0.5 kg
M_{ns}	Nominal mass of Slave	1.2 kg
K_t	Nominal thrust constant	33 N/A
K_p, K_v, K_f	Feedtback gain	6400, 160, 1.2
g_d	Gain of DOB	1000 rad/s
g_r	Gain of RFOB	1000 rad/s
–	Resolution of linear encoder	0.1 μm

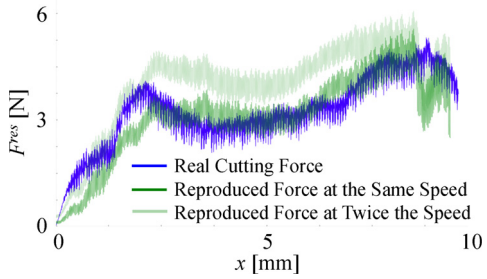

Fig. 14. Comparison with real cutting

3.5 Experimental Result An experiment was conducted to confirm the validity of the proposed method. The environment was a 10 mm-thick pine wood sample as porous as cortical bone and as dense as trabecular bone.

Figure 14 shows a comparison between the cutting-force reproduction and the real cutting. The real cutting force was obtained by cutting the environment using a bilateral control. The cutting force can be written as Eq. (19), based on the results of the previous chapter. The reproduced cutting force was simulated from Eq. (19) using the same CT number value:

$$F^{res} = s_t(A_0(C_T, \dot{x}) + B_{30}(C_T)\sin(2\pi 30t) + B_{60}(C_T)\sin(2\pi 60t)); \quad \cdots\cdots (19)$$

$$A_0(C_T, \dot{x}) = 10^{-1.35} C_T'^{0.77}(1 + 0.25\dot{x}); \quad \cdots\cdots (20)$$

$$B_{30}(C_T) = 10^{3.92} C_T'^{-1.91}; \quad \cdots\cdots (21)$$

$$B_{60}(C_T) = 10^{1.72} C_T'^{-1.29}. \quad \cdots\cdots (22)$$

In the practical use, the dental student will carry out various motions. Therefore the reproduced force will be different every time depending their cutting velocity. In this experiment, the reproduced force is force reference to the force controller and the velocity is simulated as same as real cutting for comparing the error. The reproduced force at twice the speed is also shown in the graph. The result shows that the reproduction achieved the same force response as the real cutting.

The average in absolute value of the error is 0.72 N. It is large because the amplitude of the cutting vibration is around 0.47 N and it makes the absolute error large. On the other hand, the average in the error is 0.15 N. It is only 3.5% of average value in real cutting force. It is smaller than the accuracy of 5% in the cone-beam CT [26]. And the usefulness of the proposed method was confirmed.

4. Conclusion

In this paper, a method for simulating the cutting-force response was proposed using a robotic drilling system for implant surgery. This system allows dental students to learn and practice procedures such as cutting the jaw bone. The proposed method is based on modeling the equation of cutting force and CT number using the relationship between each parameter and the density of the cutting material. The parameters of the pine wood mentioned in Misch's bone-density classification scheme were identified using the model of the cutting force from a constant-velocity experiment. The validity of the proposal was thus confirmed experimentally.

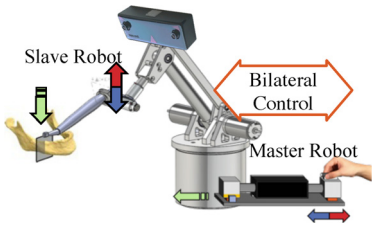

Fig. 15. Concept of the system

The proposed method can be also used for real time CT number estimation using (25) when tactile teleoperation using bilateral control, where LPF(s) is low pass filter:

$$\mathrm{LPF}(s)F^{res} = s_t A_0(C_T, \dot{x}) \quad \cdots\cdots (23)$$

$$= s_t b_{n0} C_T'^{n}(1 + K_e\dot{x}) \quad \cdots\cdots (24)$$

$$C_T' = \left(\frac{\mathrm{LPF}(s)F^{res}}{s_t b_{n0}(1 + K_e\dot{x})}\right)^{\frac{1}{n}}. \quad \cdots\cdots (25)$$

As a future work, this model will be implemented to implant surgery-supporting robot shown in Fig. 15. This robot is designed for position and angle adjustment using potential field [22]. By combing bilateral control, this robot can also achieve real-time CT number estimation and automatic stop system.

Acknowledgment

This work is supported in part by a Grant-in-Aid for the Leading Graduate School program for "Science for Development of Super Mature Society" from the Ministry of Education, Culture, Sport, Science, and Technology in Japan, and the Ministry of Education, Culture, Sports, Science and Technology of Japan under Grant-in-Aid for Scientific Research (S), JP25220903, 2013.

References

(1) R. Adell, U. Lekholm, B. Rockler, and P.I. Brånemark: "A 15-year Study of Osseointegrated Implants in The Treatment of The Edentulous Jaw", *International Journal of Oral Surgery*, Vol.10, No.6, pp.387–416 (1981)

(2) C.D.R. Kalpidis and R.M. Setayesh: "Hemorrhaging Associated With Endosseous Implant Placement in the Anterior Mandible: A Review of the Literature", *Journal of Periodontology*, Vol.75, No.5, pp.631–645 (2004)

(3) I.K. Karoussis, G.E. Salvi, L.J. Heitz-Mayfield, U. Bragger, C.H. Hammerle, and N.P. Lang: "Long-term Implant Prognosis in Patients With and Without a History of Chronic Periodontitis: a 10-Year Prospective Cohort Study of The ITI Dental Implant System", *A Clinical Oral Implants Research*, Vol.14, No.3, pp.329–339 (2003)

(4) G.H. Farnworth and J.A. Burton: "Optimization of drill geometry for orthopaedic surgery", Proc. of the 14th International Conference on Machine Tool Design and Research Conference, Manchester, England (1974)

(5) E. Jantunen: "A summary of methods applied to tool condition monitoring in drilling", International Journal of Machine Tools and Manufacture, Vol.42, pp.997–1010 (2002)

(6) J.M. Stein and D.A. Dornfeld: "Burr formation in drilling miniature holes", CIRP Annals-Manufacturing Technology, Vol.46, pp.63–66 (1997)

(7) J.L. Bassi, M. Pankaj, and S. Navdeep: "A technique for removal of broken cannulated drill-bit: Bassi's method", Journal of Orthopaedic Trauma,

Vol.22, pp.56–58 (2008)
(8) M. Price, S. Molloy, M. Solan, A. Sutton, and D.M. Ricketts: “The rate of instrument breakage during orthopaedic procedures”, International Orthopaedics, Vol.26, pp.185–187 (2002)
(9) P.N. Brett, D.A. Baker, R. Taylor, and M.V. Griffiths: “Controlling the penetrationof flexible bone tissue using the stapedotomy microdrill”, Proceedings of the Institution of Mechanical Engineers, Part I: Journal of Systems and Control Engineering, Vol.218, pp.343–351 (2004)
(10) D. Kendoff, M. Citak, M.J. Gardner, T. Stubig, C. Krettek, and T. Hufner: “Improved accuracy of navigated drilling using a drill alignment device”, Journal of Orthopaedic Research, Vol.25, pp.951–957 (2007)
(11) F.R. Ong and K. Bouazza-Marouf: “The detection of drill-bit break-through for the enhancement of safety in mechatronic assisted orthopaedic drilling”, Mechatronics, Vol.9, pp.565–588 (1999)
(12) G. Augustin, S. Davila, K. Mihoci, T. Udiljak, D.S. Vedrina, and A. Antabak: “Thermal osteonecrosis and bone drilling parameters revisited”, Archives of Orthopaedic and Trauma Surgery, Vol.128, pp.71–77 (2008)
(13) A.R. Eriksson, T. Albrektsson, and B. Albrektsson: “Heat caused by drilling cortical bone. Temperature measured in vivo in patients and animals”, Acta Orthopaedica Scandinavica, Vol.55, pp.629–631 (1984)
(14) J.E. Lee, Y. Rabin, and O.B. Ozdoganlar: “A new thermal model for bone drilling with applications to orthopaedic surgery”, *Medical Engineering and Physics*, Vol.33, pp.1234–1244 (2011)
(15) S. Kasiri, G. Reilly, and D. Tylor: “Wedge indentation fracture of cortical bone: experimental data and predictions”, *Journal of Biomechanical Engineering*, Vol.132, pp.1081–1091 (2010)
(16) P.N. Brett, C.A. Fraser, M. Hennigan, M.V. Griffiths, and Y. Kamel: “Automatic surgical tools for penetrating flexible tissues”, *IEEE Engineering in Medicine and Biology Magazine*, Vol.14, pp.264–270 (1995)
(17) C.E. Misch: “Density of bone: effect on treatment plans, surgical approach, healing, and progressive boen loading”, *The International Journal of Oral Implantology: Implantologist*, Vol.6, No.2, pp.23–31 (1990)
(18) J. Wu, G. Yu, D. Wang, Y. Zhang, and C.C.L. Wang: “Voxel-based interactive haptic simulation of dental drilling”, Proc. of the ASME 2009 International Design Engineering Technical Conferences and Computers and Information in Engineering Conference, San Diego, California, USA (2009)
(19) L. Kim and S.H. Park: “Haptic interaction and volume modeling techniques for realistic dental simulation”, Proc. of the 15th international conference on Intelligent user interfaces, Vol.22, pp.90–98 (2006)
(20) P. Rhienmora, K. Gajananan, and P. Haddawy: “Haptic Augmented Reality Dental Trainer with Automatic Performance Assessment”, The International Journal of Oral Implantology: Implantologist, New York, NY, USA (2010)
(21) Y. Kasahara, H. Kawana, S. Usuda, and K. Ohnishi: “Telerobotic-assisted bone-drilling system using bilateral control with thrust operation scaling and cutting force scaling”, *nternational Journal of Medical Robotics and Computer Assisted Surgery*, Vol.8, No.2, pp.221–229 (2012)
(22) K. Yu, K. Ohnishi, H. Kawana, and S. Usuda: “Modulated potential field using 5 DoF implant assist robot for position and angle adjustment”, In Proceedings of 41st Annual Conference of the IEEE, Yokohama, Japan (2015)
(23) Y. Matsumoto, S. Katsura, and K. Ohnishi: “Reproducibility and operationality in bilateral teleoperation”, In Proc. of the 8th IEEE International Workshop on Advanced Motion Control, Kawasaki, Japan (2003)
(24) T. Murakami, F. Yu, and K. Ohnishi: “Torque sensorless control in multidegree-of-freedom manipulator”, *IEEE Transactions on Industrial Electronics*, Vol.40, No.2, pp.259–265 (1993)
(25) G.E. Dieter: “Mechanical Metallurgy”, SI Metric ed. McGraw-Hill Book Company, UK (1988)
(26) M. Loubele, F. Maes, F. Schutyser, G. Marchal, R. Jacobs, and P. Suetens: “Assessment of bone segmentation quality of cone-beam CT versus multislice spiral CT: a pilot study”, *Assessment of bone segmentation quality of cone-beam CT versus multislice spiral CT: a pilot study*, Vol.102, No.2, pp.225–234 (2006)

Koyo Yu (Non-member) received the B.E. degree in system design engineering, the M.E. degree in integrated design engineering, and the M.P.A.S degree in medical sciences from Keio University, Yokohama, Japan, in 2012, 2014, and 2015, respectively, where he is currently working toward the Ph.D. degree in Keio University. His research interests include physician support using haptics.

Takuya Matsunaga (Student Member) received the B.E. degree in system design engineering and the M.E. degree in integrated design engineering from Keio University, Yokohama, Japan, in 2014 and 2015, respectively, where he is currently working toward the Ph.D. degree in Keio University. His research interests include motion control, haptics, robotics, and surgical robot.

Hiromasa Kawana (Non-member) graduated from Tohoku University Graduate School of Dentistry, Tohoku, Japan, in 1988. He worked in Johannes Gutenberg University, Mainz, Germany as a visiting researcher from 1993 to 1994. Now he is a associate professor of department of dentistry and oral surgery, Keio University.

Shin Usuda (Non-member) graduated from Tokyo Dental College, Tokyo, Japan, in 2004. He worked in Tokyo Metropolitan Cancer and Infectious Diseases Center Komagome Hospital in 2007. Currently, he works as a director oral surgery at the Tachikaw Hosipital.

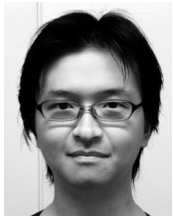

Kouhei Ohnishi (Fellow) received the B.E., M.E., and Ph.D. degrees in electrical engineering from The University of Tokyo, Tokyo, Japan, in 1975, 1977, and 1980, respectively. Since 1980, he has been with Keio University, Yokohama, Japan and is now a Professor of Department of System Design Engineering. His research interests include motion control, robotics, and haptics.